On the Electrolyte Convection around a Hydrogen Bubble Evolving at a Microelectrode under the Influence of a Magnetic Field

Dominik Baczyzmalski,[a,z] **Franziska Karnbach,**[b,c] **Xuegeng Yang,**[d] **Gerd Mutschke,**[d,e]
Margitta Uhlemann,[c] **Kerstin Eckert,**[d] **and Christian Cierpka**[a]

[a]*Institute of Fluid Mechanics and Aerodynamics, Universität der Bundeswehr München, D-85577 Neubiberg, Germany*
[b]*Faculty of Mechanical Science and Engineering, TU Dresden, D-01062 Dresden, Germany*
[c]*IFW Dresden, Institute for Complex Materials, D-01171 Dresden, Germany*
[d]*Institute of Fluid Mechanics, Technische Universität Dresden, D-01069 Dresden, Germany*
[e]*Helmholtz-Zentrum Dresden - Rossendorf, Institute of Fluid Dynamics, D-01328 Dresden, Germany*

Water electrolysis was carried out in a 1 M H_2SO_4 solution under different potentiostatic conditions in the presence of a magnetic field oriented normal to the horizontal microelectrode (100 μm in diameter). The imposed magnetohydrodynamic (MHD) electrolyte flow around the evolving hydrogen bubble was studied to clarify the effect on the detachment of the bubble from the electrode and the mass transfer toward the electrode. Different particle imaging and tracking techniques were applied to measure the three-dimensional flow in the bulk of the cell as well as in close vicinity of the evolving bubble. The periodic bubble growth cycle was analyzed by measurements of the current oscillations and microscopic high-speed imaging. In addition, a numerical study of the flow was conducted to support the experimental results. The results demonstrate that the MHD flow imposes only a small stabilizing force on the bubble. However, the observed secondary flow enhances the mass transfer toward the electrode and may reduce the local supersaturation of dissolved hydrogen.

Renewable energy technologies have become increasingly important in view of the worldwide rising CO_2 emissions. The growing application of volatile energy sources such as wind and solar power requires efficient energy storage and distribution systems in order to sustain stability in the electrical grid. Hydrogen shows great potential for long-term energy storage as well as mobile units employing fuel cells as it provides a large energy density. Moreover, high purity hydrogen (and oxygen) can be directly generated from the electricity produced by a wind turbine or solar panel by the electrolysis of water. However, one main challenge for the establishment of water electrolysis on an industrial scale is its relatively low efficiency, typically in the order of 60% for conventional alkaline water electrolyzers.[1]

A considerable part of the losses is the result of hydrogen and oxygen gas bubbles evolving at, and sticking to the electrodes' surfaces, thus hindering the formation of new gas bubbles. Furthermore, they reduce the effective electrical conductivity of the electrolyte, which leads to an increased ohmic voltage drop. The accelerated removal of gas bubbles from the electrode's surface and the bulk was studied by many researchers to improve the efficiency of the process.[2–6] Forced convection has been found to be able to enhance the detachment of bubbles from the electrode and therefore reduce the fractional bubble coverage significantly.[7–12] A relatively simple method that has recently attracted considerable research interests in this context is the application of magnetic fields. The superposition of a magnetic field on the inherent electric field gives rise to Lorentz forces $\mathbf{f_L} = \mathbf{j} \times \mathbf{B}$ acting as body forces directly on the electrolyte, where $\mathbf{j}$ denotes the current density and $\mathbf{B}$ is the magnetic induction, respectively.[13] The flow generated by these Lorentz forces is often referred to as the magnetohydrodynamic (MHD) effect.

It was shown that stirring with Lorentz forces reduced the ohmic losses and overpotentials in alkaline and acidic environments.[14,15] Moreover, a reduced void fraction in the electrode gap and a lower bubble coverage on large electrodes was observed for increasing magnetic field strengths and thus increasing magnitudes of the Lorentz force in the case of an electrode-parallel magnetic field.[16,17] Koza et al.[18–20] showed that both the bubble size and the fractional bubble coverage on large planar electrodes were decreased by the application of magnetic fields, irrespective of the magnetic field orientation. The MHD convec-tion in an electrode-parallel field is characterized by a strong shear flow with high flow velocities close to the electrode surface as shown by measurements of the velocity field in the electrode gap of an alkaline electrolyzer.[21,22] Thus, the enhanced bubble detachment for parallel fields was generally attributed to the effect of the strong MHD convection along the electrode, similar to the findings of other studies investigating the bubble detachment dynamics under forced convection.[23,24] However, the situation for a magnetic field perpendicular to the electrode is unclear. It was assumed that the Lorentz-force-induced flow forms a region of lower pressure above the bubble, thus introducing a force in the same direction as buoyancy.[20] However, recently it was suggested that this additional lift force is several orders of magnitude lower than the buoyancy force and thus probably not responsible for the observed enhanced detachment.[25] Consequently, a better understanding of the complex three-dimensional flow around the evolving bubbles is still necessary to reveal the underlying mechanisms.

Unfortunately, it is almost impossible to experimentally investigate a single bubble that may form on random places all over the electrode. Therefore, researchers have chosen nano-[26] or microelectrodes (diameter ∼ $O(100 \,\mu m)$) to pin the bubbles at a certain position.[27–30] In contrast to the case of large working electrodes, experimental[29,28] and numerical[31] investigations at microelectrodes point to a stabilizing effect of the magnetic field on the bubbles. Indeed, with increasing Lorentz force, the growth rate of the bubbles became smaller and the bubbles remained attached longer on the electrode before they detached. This was attributed to a changed Lorentz force distribution on a microelectrode, forming a low pressure region in the lower part of the bubble as opposed to the case of a macroelectrode.[31] This is a consequence of the electric field lines, which are strongly bent and concentrated in the vicinity of the microelectrode (see Fig. 2), As a result, much higher Lorentz forces are generated in the lower part of the bubble and give rise to a stronger azimuthal flow and pressure decrease in this region. However, detailed investigations of the MHD flow and the pressure distribution around the bubble are not sufficiently available yet, but are crucial to clarify the effect of a pressure-related stabilizing force and gain insight into further relevant effects of the complex flow such as mass transfer and interfacial phenomena. Therefore, the aim of the current study is to resolve some of these issues by providing for the first time both electrochemical measurements and extensive time-resolved three-dimensional velocity measurements of the electrolyte flow in the bulk and in the vicinity

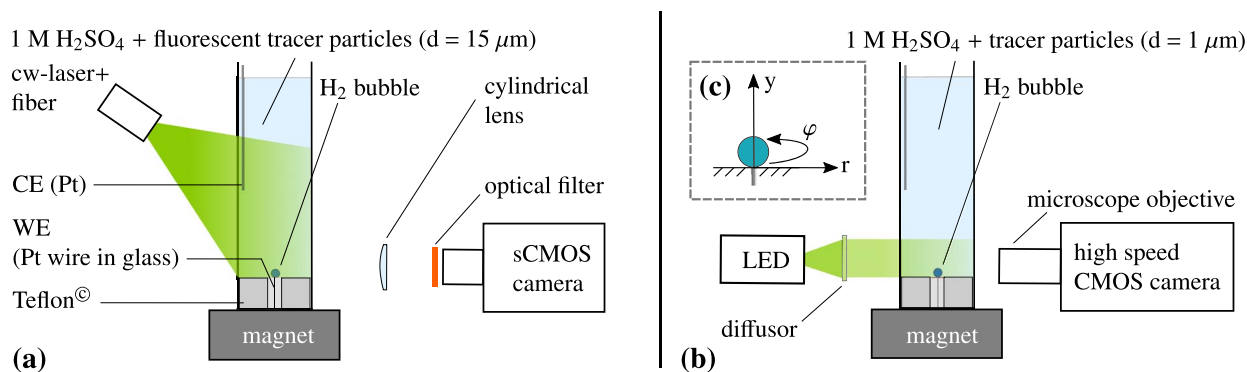[z]E-mail: Dominik.Baczyzmalski@unibw.de

Figure 1. Sketch of experimental setup: APTV measurements for the three-dimensional volumetric velocity field in the bulk (a) and 2D shadowgraph measurements for the bubble geometry and the 2D velocity field near the bubble (b). The applied coordinate system is illustrated on the right hand side in (c).

of a hydrogen bubble evolving at a microelectrode under the influence of an electrode-normal magnetic field. The bubble growth dynamics and the bubble-induced velocity field in the absence of a magnetic field has already been studied thoroughly by Yang et al.[27] for the same electrochemical cell that was used here. Thus, the focus of the current investigation lies on the effects of the magnetic field and the generated Lorentz forces, which were varied by operating the cell under different potentials and applying a permanent magnet.

The paper is organized as follows. First, the experimental setup including the methods for the three-dimensional velocity measurements, bubble radius determination and numerical simulation are explained. The results of the bubble evolution are shown in next section, followed by the discussion of the bulk flow and the near-bubble flow. The findings are finally summarized in the last section.

Experimental and Numerical Methods

Electrochemical setup.—A cuboid glass cuvette (Hellma, $45 \times 10 \times 10$ mm^3 [H × W × D]) with a 3-electrode setup[27] was used to periodically generate single H$_2$ bubbles in a 1 M H$_2$SO$_4$ solution (Fig. 1). The working electrode of the electrochemical cell was made from a Pt wire with a diameter of 100 μm and a purity of 99.99%. The Pt wire was burned into a glass capillary and polished with SiC grinding papers ending with grid #4000. It should be mentioned that the quality of the surface preparation plays an important role for the reproducibility of the results. No polishing suspensions were used that could adsorb or absorb on the Pt surface and influence the bubble behavior. The glass capillary was embedded in a Teflon plate. The bottom of the glass cuvette was cut in order to mount the cell on the Teflon plate with the embedded Pt wire. A copper block with a drilled hole inside was placed below the Teflon plate to enable contact to a potentiostat. The hole was filled with Field's metal which was firmly connected with the working electrode. Another Pt wire with a diameter of 1 mm served as the counter electrode. A mercury/mercurous sulfate electrode (MSE; 650 mV vs. SHE), connected through a salt bridge filled with electrolyte, was used as reference electrode.

A magnetic field was superimposed normal to the electrode surface using a NdFeB magnet ($20 \times 40 \times 40$ mm^3 [H × W × D])), which was centrally attached below the Teflon plate. The distance between the upper side of the magnet and the cathode was 14 mm. The magnetic induction B was 180 mT on the surface of the working electrode and decayed rapidly with increasing height. The resulting Lorentz force density $f_L = j \times B$ points in azimuthal direction (see Fig. 2).

Water electrolysis was conducted under potentiostatic conditions at −1.2 V, −1.5 V and −2.0 V with respect to MSE using a Zahner Zennium electrochemical workstation. The current transient during the bubble growth was measured in parallel for each set of experiments described below. Before running experiments, the glass cuvette and the Teflon plate were cleaned with Caro's acid and rinsed with deionized water carefully to avoid any influence of organics.

Measurements of the liquid phase velocity and bubble geometry.—In order to characterize the MHD flow around the growing bubble, two different experimental arrangements were used (Fig. 1). The first set of experiments was designed to investigate the three-dimensional velocity field in the bulk of the electrochemical cell. Astigmatism Tracking Velocimetry[32] (APTV), which is a single camera three-dimensional volumetric particle tracking technique, was applied as illustrated in the left part of Fig. 1. Fluorescent polysterene tracer particles (FluoRot, $d_p = 15$ μm, microParticles GmbH) were added to the H$_2$SO$_4$ solution and illuminated by a solid state laser (532 nm, 2 W optical power) via an optical fiber. The electrophoretic velocity for the particles in the electric field was estimated to be in the order of 10^{-3} mm/s (three orders of magnitude smaller than the measured velocities) and can thus be neglected.[33] The light emitted by the fluorescent particles was captured by a sCMOS camera (PCO.edge by PCO GmbH) at a frame rate of 30 fps with a magnification of about $M = 1$. An additional 532 nm notch filter allowed the particle images to be recorded without laser light reflections from the gas bubbles and the glass walls. Moreover, a cylindrical lens with a focal length of f = 300 mm was placed in front of the camera to create astigmatic distortions of the particle images. As a result, the particle images become ellipsoidal, and by a proper calibration[34] the size of the major and minor axis can be used to determine the depth position of the respective particles. The position of the particle image in the XY-plane is obtained from the centroid of the particle image as in the case of conventional particle image tracking (PTV) techniques. The resulting spatial resolution in the XY-plane was about 165 pixel/mm and 150 pixel/mm in the X- and Y-direction, respectively. A particle tracking algorithm[35] was used to determine the particle paths from successive images. Since the 3D positions of the particles in the volume are known, the full
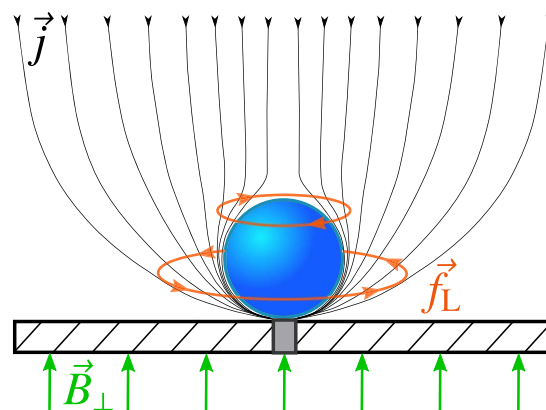

Figure 2. Schematic illustration of the current distribution $\vec{j}$ around the hydrogen bubble and the direction of the Lorentz forces $\vec{f}_L$ resulting from a magnetic field $\vec{B}_\perp$ oriented normal to the electrode.

three-dimensional three-component (3D3C) velocity vector can be obtained by this method.

In order to characterize the flow in the vicinity of the growing bubble as well as the bubble geometry, a much higher magnification of $M = 23$ was applied in the next set of experiments by using a high speed camera with a microscope objective (Fig. 1b). Simultaneous measurements of the growing bubble and the 2D velocity field were achieved using polystyrene tracer particles with a diameter of 1 μm and visualizing both the bubble and the particles by means of shadowgraphy. The background illumination was provided by a LED operating in the green wavelength range (Lumencor SPECTRA X light engine) and a diffuser at the rear wall of the cell. The measurements were carried out at a frame rate of 100–200 fps with a high speed camera (PCO DIMAX by PCO GmbH). The resolution was set to 2.1 pixel/μm. The 2D velocity field was obtained from the shadow images by applying image processing and PTV techniques. For the latter, a probabilistic tracking algorithm was used.[36] Moreover, the bubble geometry was extracted from the shadow images by image processing, detection of the bubble image and fitting an ellipse through its edge points.

Flow evaluation methods.—Given the spherical shape of the evolving bubbles and the rotating nature of the flow imposed by the Lorentz forces, a cylindrical r-y-φ-coordinate system was chosen. Here, r, y and φ denote the radial, vertical and azimuthal coordinate with respect to the center of the microelectrode, respectively (Fig. 1c). The bulk flow was characterized by means of time-averaging the three-dimensional APTV data. For this purpose the data was segmented in bins with a size of 250×250 μm^2 and 2π (entire circumference) in the r-y-plane and φ-direction, respectively. The binned data of two consecutive measurements, each of them comprising the periodic evolution of about 100 bubbles, was used for the time-averaging.

The flow near the growing bubble was characterized by phase-averaging the PTV data obtained from the 2D shadowgraphy measurements. Since the spatial resolution was higher compared to the APTV measurements, smaller bin sizes of 15×15 μm^2 were chosen to resolve the flow around the periodically evolving bubble. Prior to the phase-averaging, the time instants of each individual bubble evolution cycle and their corresponding residence time on the electrode surface were determined from the high-speed images and the time difference between the current peaks associated with the bubble evolution cycle (see Fig. 4), respectively. This way, the phase-averaging of the PTV data was realized by dividing the evolution process of each bubble into 20 equally spaced time intervals or phases, assigning the time-resolved PTV data of each bubble to the corresponding phases and averaging the resulting data. The bubble geometry and its position were also phase-averaged to allow for a combined display of the phase-resolved bubble and the surrounding flow. Depending on the configuration studied, a number of 75–200 bubbles with a nearly constant lifetime was used for the phase-averaging, thus providing for sufficient statistics and a better spatial coverage of velocity vectors in comparison to a time-resolved evaluation for a single bubble. In addition, a common outlier detection algorithm[37] was applied on both the APTV and the 2D PTV, to reduce the amount of spurious vectors.

For most of the 2D high resolution measurements, the measurement plane was located in the center of the bubble and, assuming rotational symmetry of the imposed flow, served to determine the velocity field in the r-y-plane. In addition, the measurement plane was moved closer to the camera by a distance of 130 μm and 330 μm, respectively, to visualize the azimuthal velocity component of the rotating flow. The particle displacement in this plane will display the projection of the velocity vector in that plane. Nevertheless, in order to determine the 3C velocity field, the actual azimuthal component could be reconstructed from the 2D velocity field by assuming that the flow is rotationally symmetrical and that the position of the bubble center with respect to the measurement position is known. The measurement results show that these are valid assumptions and help to visualize and understand the complex three-dimensional flow.
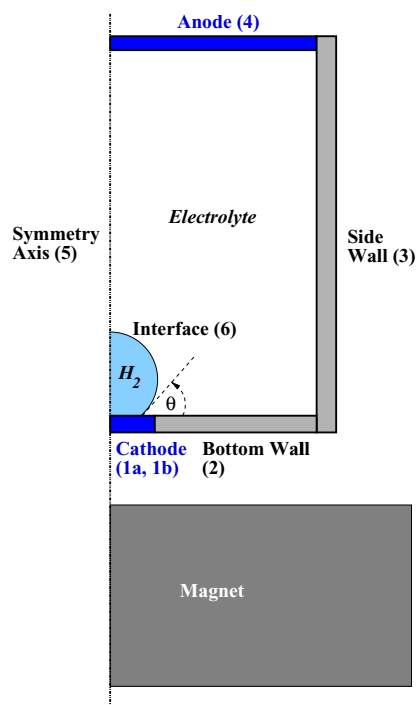

Figure 3. Sketch of the cylindrical cell geometry (scales are modified for better visibility) shown in the (r, y)-plane with numbered boundary segments to explain the conditions applied in the numerical simulation.

Numerical model.—In order to gain further insight, finite element simulations were performed for the electrolysis process with a stationary hydrogen bubble attached to the microelectrode. The simulations were set up to closely match the experimental conditions and took into account the action of the Lorentz force as well as the mass transfer at the bubble-liquid interface during electrolysis. For simplicity, a cylindrical cell was used which allows to assume azimuthal symmetry in the simulations (see Fig. 3). The radial extension of the cell (R_C) and of the permanent magnet (R_M) were set to maintain the respective horizontal cross-sectional areas, thus keeping the respective aspect ratios of height to width approximately constant. For the permanent magnet (40×40 mm^2) and the cell (10×10 mm^2) $R_M = 22.57$ mm and $R_C = 5.643$ mm were used, respectively. The calculation of the magnetic field **B** decouples from the rest of the problem and can be performed as a preprocessing step. Here, a much larger spherical domain than shown in Fig. 3 was used to avoid any influence of the outer boundary.[38] Using the vertical distance between the cathode surface and the upper magnet surface of the experiment, a magnetic induction of 181 mT was obtained at the electrode surface, which is in very good agreement with the measured value of 180 mT. As the radial dimension of the magnet is large compared to the cell radius, the magnetic field orientation is almost perfectly vertical in the lower cell region, although the modulus of **B** is decreasing with height. The steady simulations performed mimic the experimental conditions for E = -1.5 V under the influence of the magnetic field at two different characteristic phases: at an early phase of the bubble growth ($\tau = 0.15$) and close to detachment ($\tau = 0.9$). Here, τ denotes the non-dimensional time scale of the bubble growth cycle from nucleation ($\tau = 0$) to detachment ($\tau = 1$). For $\tau = 0.15$ and $\tau = 0.9$, circular bubble shapes with a respective radius of 145 μm and 235 μm and a contact angle of 9° and 5° were assumed according to the data of Yang et al.,[27] which were obtained for the same electrochemical cell. This yields a covered electrode radius of about 22.7 μm and 20.5 μm, respectively. Assuming a constant electrical conductivity σ of the electrolyte (1 M H$_2$SO$_4$) and a non-conductive gaseous phase, the primary current density **j** in the electrolyte was determined by solving a Laplace equation for the electric potential Φ

$$\Delta \Phi = 0, \qquad \mathbf{j} = \sigma \nabla \Phi \qquad [1]$$

For potentiostatic operation, the respective boundary conditions at the electrodes (1,4) can be set such as to match the desired cell current of the experiment. Hereby, at the cathode, only the wetted part (1b) is to be used, whereas at the remaining walls (2,3) and at the bubble interface (6) no-flux conditions $\partial j/\partial n = 0$ apply (n denotes the respective normal direction). As inertial effects of the Lorentz force can approximately be neglected in a first step, steady simulations were performed in the following. The concentration of dissolved hydrogen c in the electrolyte is obtained from solving a respective steady convection-diffusion equation

$$(\mathbf{u}\nabla)c = D\,\Delta c \qquad [2]$$

Here, $\mathbf{u}$ and D denote the velocity vector of the electrolyte and the diffusion coefficient of the dissolved hydrogen, respectively. The distribution of the current density at the wetted part of the cathode (1b) is used to define the boundary flux describing the production rate of dissolved hydrogen. By using Faraday's law, it reads

$$\frac{\partial c}{\partial n} = \frac{j_n}{zFD} \qquad [3]$$

where n, z and F denote the electrode-normal direction, the charge number and the Faraday constant, respectively. The boundary condition at the bubble interface (6) was defined according to thermodynamic equilibrium by using Henry's law, $c_{sat} = k_H p$, where k_H denotes the Henry constant and p the pressure in the hydrogen bubble. Mass transfer occurs if the electrolyte concentration next to the interface differs from the saturation concentration c_{sat}. At the bottom wall (2), a no-flux condition was applied, whereas at the side wall (3) and at the anode (4) the hydrogen concentration was set to zero. The simulation of the electrolyte flow was conducted by solving the incompressible Navier-Stokes equations, which include the Lorentz force $\mathbf{f_L} = \mathbf{j} \times \mathbf{B}$ defined earlier and the buoyancy force $\mathbf{f_B}$ within the Boussinesq approach.

$$\rho_0\,(\mathbf{u}\nabla)\,\mathbf{u} = -\nabla p + \eta\,\Delta\mathbf{u} + \mathbf{f_L} + \mathbf{f_B},$$
$$\mathbf{f_B} = \rho_0\,\beta_c\,(c - c_0)\,\mathbf{g}, \qquad [4]$$
$$\nabla \cdot \mathbf{u} = 0$$

Density changes occur due to changes of composition of the electrolyte, whereby c, β_c, ρ_0 and η denote the concentration of dissolved hydrogen, the volume expansion coefficient, the bulk density and the dynamic viscosity of the electrolyte, respectively. The last equation denotes the incompressibility constraint. Inside the hydrogen bubble, Equation 4 with corresponding material parameters (ρ_H, η_H) was used, whereby the Lorentz force and the buoyancy force in Eq. 4 vanish. At all boundaries (1-4), a no-slip condition $\mathbf{u} = 0$ was applied. At the liquid-gas interface (6), a slip-condition was used to allow for convection inside the bubble and motion of the interface. By applying Eq. 4 at the interface it then follows $u_n^{(H)} = u_n = 0$ and $\mathbf{u}_t^{(H)} = \mathbf{u}_t$, where $\mathbf{u}_t$ denotes the respective tangential velocity vector at the interface. At the symmetry axis (5) at $r = 0$, respective symmetry conditions for all the equations to be solved (1, 2, 4) were applied. The simulations were performed using Comsol V.4.4 with an unstructured grid of triangular elements, which during resolution studies was properly refined near the interface (6), the cathode (1) and further regions of the computational domain where large gradients of the calculated quantities occur. The resulting element size at, e.g., the cathode was 1 μm, and the final grid consisted of about 50,000 elements in total. The fully-coupled solver used in the simulation is based on a damped Newton method, yielding at convergence a weighted relative error of the solution of 10^{-5}.[39]

Results and Discussion

Bubble growth.—The operation of the electrochemical cell under potentiostatic conditions leads to a periodic generation of hydrogen bubbles on the Pt microelectrode and is accompanied by periodic oscillations of the electric current. This is exemplified in Fig. 4, which shows the current transient together with a few corresponding bubble
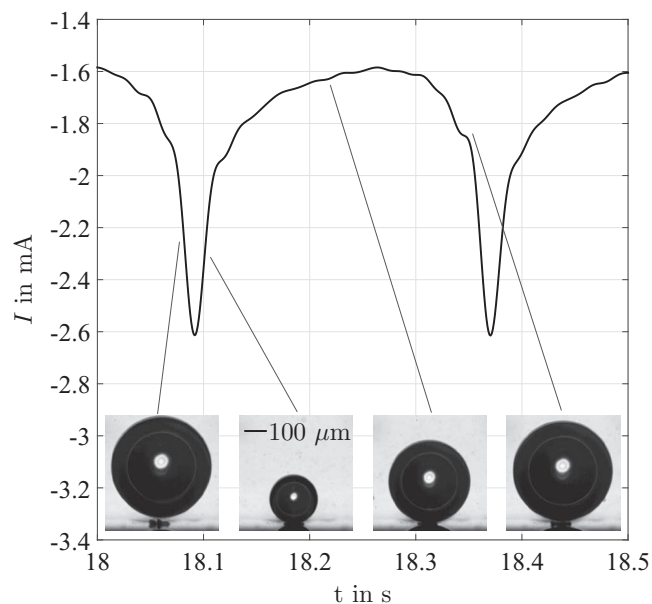
Figure 4. Zoom into the current transient I and corresponding bubble images obtained by microscopy for one period of the bubble generation conducted at E = −1.5 V and $B_\perp$ = 180 mT.

images for one period of the H_2 generation process. The detachment of the preceding bubble is immediately followed by the formation of much smaller bubbles which coalesce rapidly to one larger bubble already on the electrode.[27] The absolute value of the current is the highest in the beginning of the bubble evolution process and decreases as the bubble grows. This is due to a reduction of the active electrode area, leading to a change of the current distribution and an increase of the resistance.[28] At about 60% of the entire residence time of the bubble at the electrode, the absolute value of the current starts to increase again while the bubble continues to grow until it is able to detach from the electrode and the evolution process starts all over again. It was suggested that the increase of the current in the final stages of the bubble growth is associated with a translation of the bubble along the electrode surface[27] or small electrolyte channels[28] forming in the interface between the bubble and the electrode surface, thus increasing the active electrode area.

Fig. 5a depicts the evolution of the bubble diameter obtained from the bubble shadow images during measurement periods of 30 s at different potentials E and under a magnetic field with $B_\perp$ = 180 mT. A zoomed view of the corresponding current oscillations i is shown in Fig. 5b. It can be clearly seen from Fig. 5a, where all individual bubble data is plotted, that the diameter of each bubble generated within the measurement period of 30 s shows little scattering during the entire evolution cycle, irrespective of the applied potential. Similarly, the lifetime or the residence time of the bubble on the electrode surface remained nearly constant as was confirmed by calculating the time difference of the associated current peaks (not illustrated). Thus, for short polarization times of $t = 30$ s the phase-averaged flow fields discussed later can be considered to be a reasonable representation of the flow around each of these bubbles.

The bubble is growing faster for increasing potentials as illustrated in Fig. 5a. This is a direct consequence of the higher absolute value of the current (see Fig. 5b), which is almost completely converted into hydrogen gas.[27] Hence, the observed bubble diameter follows a $d \propto t^{1/3}$ dependency as reported in other studies.[27,29,40] Furthermore, it can be seen from Fig. 5 that the bubble residence time at the electrode is nearly the same for potentials of E = −1.2 and −1.5 V, but increases for E = −2 V.

Bulk flow.—The resulting time-averaged three-dimensional velocity fields in the electrochemical cell operated at different potentials
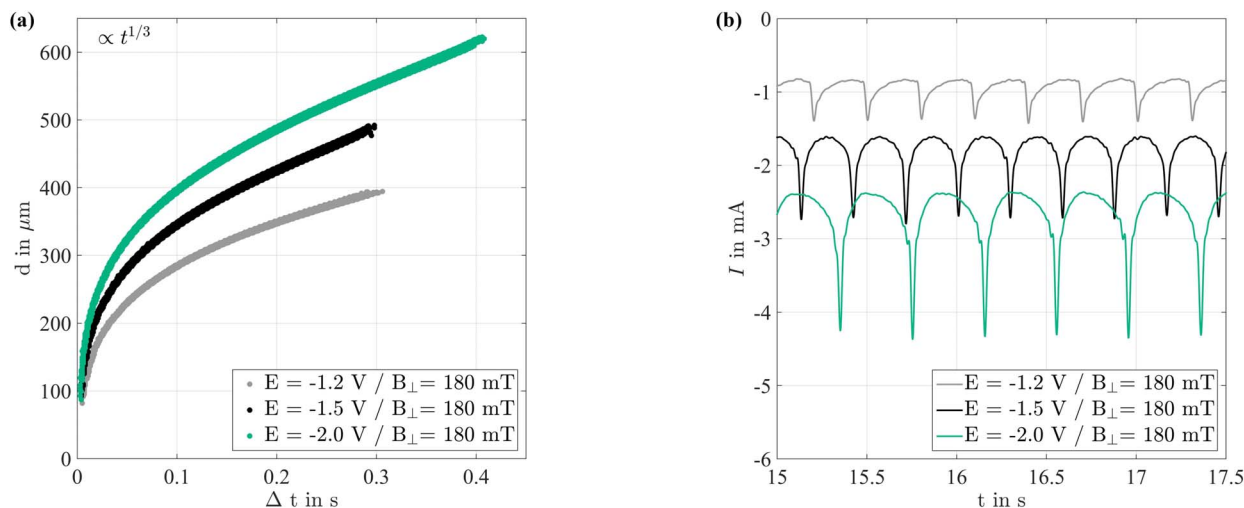
Figure 5. (a) Evolution of bubble diameter d under a magnetic field with $B_\perp = 180$ mT for different potentials E and measurement periods of 30 s (75–100 bubbles). Δt in (a) refers to the time that passed since the nucleation of the respective bubbles. (b) Zoom into corresponding current transients I.

under the influence of the magnetic field with $B_\perp = 180$ mT are illustrated in Fig. 6. In general, the Lorentz forces act only in close vicinity of the bubble where the current field lines are bent and the magnetic field is strong (see Fig. 2). Despite this fact the Lorentz-force-driven convection reaches far into the bulk due to the viscosity of the fluid as can be clearly seen from the time-averaged azimuthal velocity field below $y = 3$ mm (Fig. 6, top). As shown in Fig. 5b, the cathodic current increases for higher cathodic potentials, thus giving rise to higher Lorentz forces. Consequently, an increase in the applied cathodic potential leads to higher magnitudes of the azimuthal convection in the bulk with the maximum observed azimuthal velocity V_φ ranging from 1.6 mm/s to 3.5 mm/s for a potential of E = -1.2 V and -2.0 V, respectively (see Fig. 6, top).

In the meridional (r-y) plane illustrated in the lower part of Fig. 6, the effect of both the bubble-driven convection and the secondary flow induced by the azimuthal MHD flow can be seen. At the lowest potential of E = -1.2 V, the meridional flow is clearly governed by the rising motion of the detached bubbles. Each bubble displaces fluid at its front side and entrains fluid at its rear side during its upward movement,[27] which is commonly referred to as the wake of the bubble. In the time-averaged sense, only the entrainment by the wake of the rising bubbles can be seen. The electrolyte is accelerated from the outside toward the center of the cell, from thereon following the vertical motion of the rising bubble. Since the bubble is accelerating after the detachment, the wake becomes stronger with increasing wall-normal distance y and requires a longer time-period to decay.

As the potential is increased, the entrainment by the wake of the rising bubbles is still visible in the upper part of the cell. An evidently different picture emerges in the lower part of the cell as the fluid is subjected to a centrifugal acceleration V_φ^2/r due to the MHD-induced azimuthal motion. This radially outward directed acceleration is able to overcome the counteracting entrainment effect of the wake induced by the previously detached bubble. Thus, a secondary flow in the form of a large vortex is established as indicated by the streamlines in the top part of Fig. 6. A similar flow effect was also reported for the copper deposition in seemingly parallel electric and magnetic fields.[41] At a potential of E = -2.0 V, the resulting vortex becomes larger due to higher Lorentz forces and extends, in a time-averaged sense, to the vicinity of the electrode. Consequently, provided that the generated Lorentz forces are high enough for the MHD secondary flow to predominate the bubble-induced electrolyte flow, such effect might enhance the mass transfer between the electrolyte in the bulk and the near-electrode region as indicated by other researchers.[14,31]

Near-bubble flow.—Fig. 7 provides an insight into the phase-averaged azimuthal flow field for different characteristic phases of the bubble evolution cycle. These velocity fields were reconstructed from the 2D *high resolution measurements* (see Fig. 1b) with the measurement plane located 130 µm and 330 µm in front of the center of the electrode, respectively. The position of these planes was chosen to have a good compromise between accuracy and reconstruction ability. The velocity fields from both reconstructions are in good agreement as can be seen at the connecting line in Fig. 7.

As indicated in Fig. 2, the direction of the generated azimuthal Lorentz force is opposite in the lower and upper half of the bubble due to the orientation of the distorted current field lines. However, only an azimuthal flow in one direction could be observed in the investigated field of view. The azimuthal velocity distribution is clearly governed by the Lorentz forces generated beneath the equator of the bubble and extends far into the bulk as shown before (see Fig. 6). This is the result of the high current density and the strong curvature of the electric field lines at the foot of the bubble.[31] In addition, the magnetic induction B is the largest at the bottom of the cell and decays rapidly with the wall-normal distance y. Consequently, the generated Lorentz forces are significantly higher on the lower part of the bubble.

As the Lorentz forces become stronger toward the foot of the bubble the azimuthal flow velocities increase as well (see Fig. 7). This increase is evidently limited by the wall, which decreases the velocity toward the wall to satisfy the no-slip condition. Moreover, the highest azimuthal velocities are reached in close vicinity of the bubble's surface. In view of the decelerating effect of a stationary wall, this result is compatible only with a mobile gas-liqiud interface as opposed to a rigid boundary with a no-slip condition as assumed in other numerical studies.[20,31] An immobilization of the interface usually occurs under certain flow conditions where surface-active solutes (surfactants) accumulate non-uniformly at the interface. The resulting surface concentration distribution leads to surface tension gradients which in turn cause a tangential stress on the bubble surface that is opposed by the surrounding flow and thereby tends to retard the interfacial motion.[42,43] Another notable aspect is the fact that the measured azimuthal velocities ($V_\varphi < 6$ mm/s, see Fig. 7) are two orders of magnitude smaller than those computed by Liu et al.[31] ($V_{\varphi max} \approx 400$ mm/s). This significant discrepancy cannot be explained by the differences in the experimental conditions but might be the result of an overestimated current density at the foot of the bubble in the numerical simulation.

As can be seen from the phase-resolved velocity fields, the azimuthal velocity is the largest in the early stages of the bubble growth cycle and extends over a large area around the bubble (see Fig. 7,
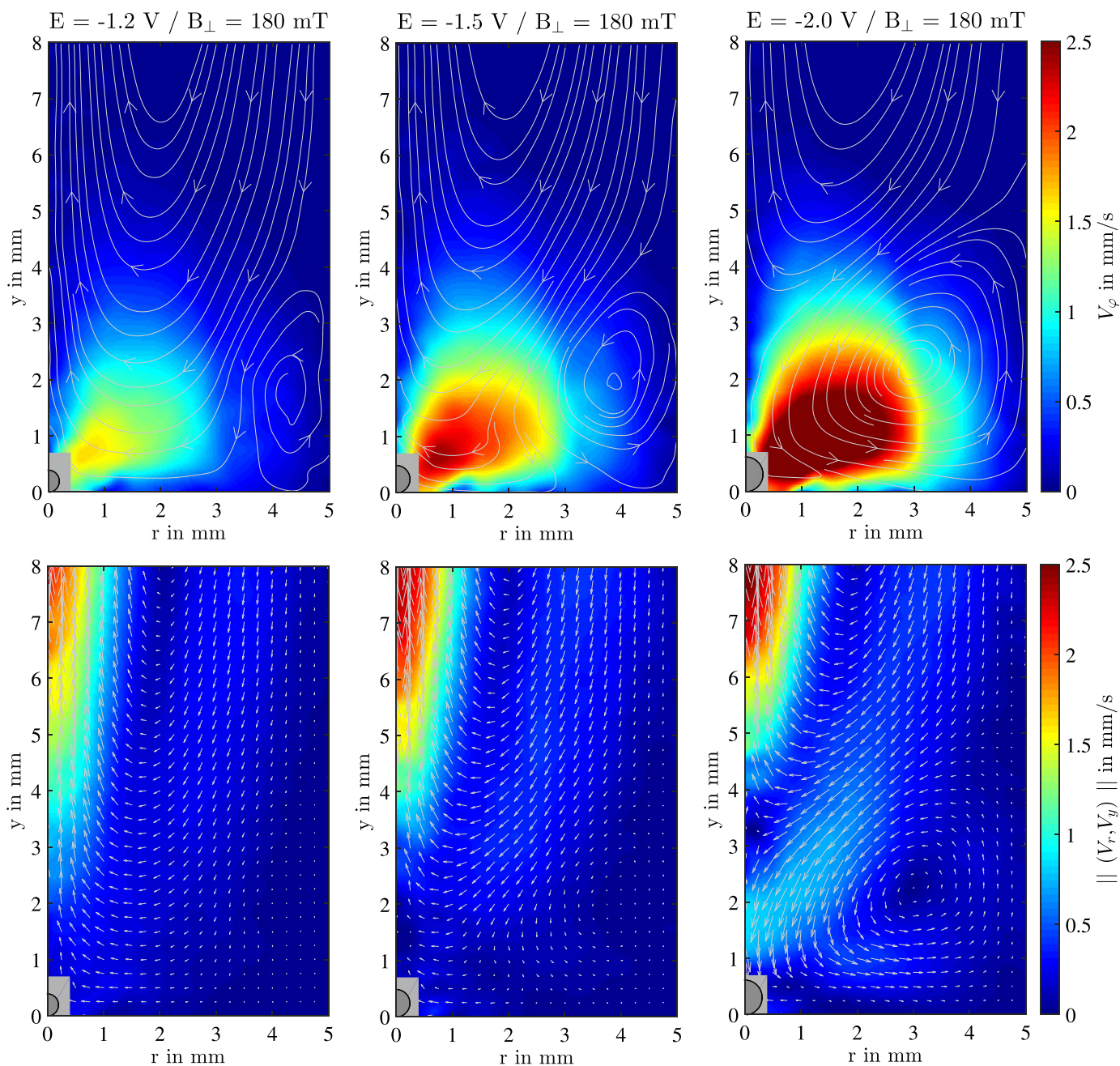
Figure 6. Time-averaged field of the azimuthal velocity component (V_φ, top) and the velocity components in the meridional (r-y) plane (V_r, V_y, bottom) in the presence of a magnetic field for different applied potentials, increasing from left to right. The streamlines in the top part are derived from the velocity field in the r-y-plane. The typical bubble shape and position at the moment of detachment (maximum diameter) were additionally indicated. The region in close vicinity of the electrode was masked out as the high resolution measurement results shown in Figs. 7 and 10 better resolve this region.

$\tau = 0.15$). As the bubble grows, the maximum azimuthal velocity near the bubble decreases at first and increases again in the later phases of the bubble growth. This behavior is directly linked to the changing magnitude of the Lorentz forces, which scales with the radial component of the current density and is therefore, in a first approximation, proportional to the change of the current. Fig. 8 compares the evolution of the normalized cathodic current $|I|/|I|_{min}$ to the time-dependent maximum of the observed azimuthal velocity, which was normalized according to its value at the minimum cathodic current. This plot shows that the maximum azimuthal velocity follows the current for $\tau > 0.3$ as the current change is moderate during these phases. In contrast, the velocity change for $\tau < 0.3$ lags behind the rapidly decreasing current due to inertial effects as the flow adapts to the sud-

den Lorentz force decrease[e]. Thus, depending on the rate of change of the local Lorentz forces and the bubble growth rate, the time response of the flow can significantly affect not only the maximum velocities but the entire instantaneous velocity field. The Lorentz force distribution around the bubble changes according to the changing current and current field distortions during the bubble growth. As a result, the strong initial azimuthal flow distribution resulting from the early growth phases decays and adapts to the changing Lorentz force distribution, which leads to a reduction of the azimuthal velocities in the

[e]Note that the velocity field was not resolved below $\tau < 0.15$ as the frame rate of the camera was optimized for the later phases where the the strong convection induced by the wake of the preceding bubble is less important.
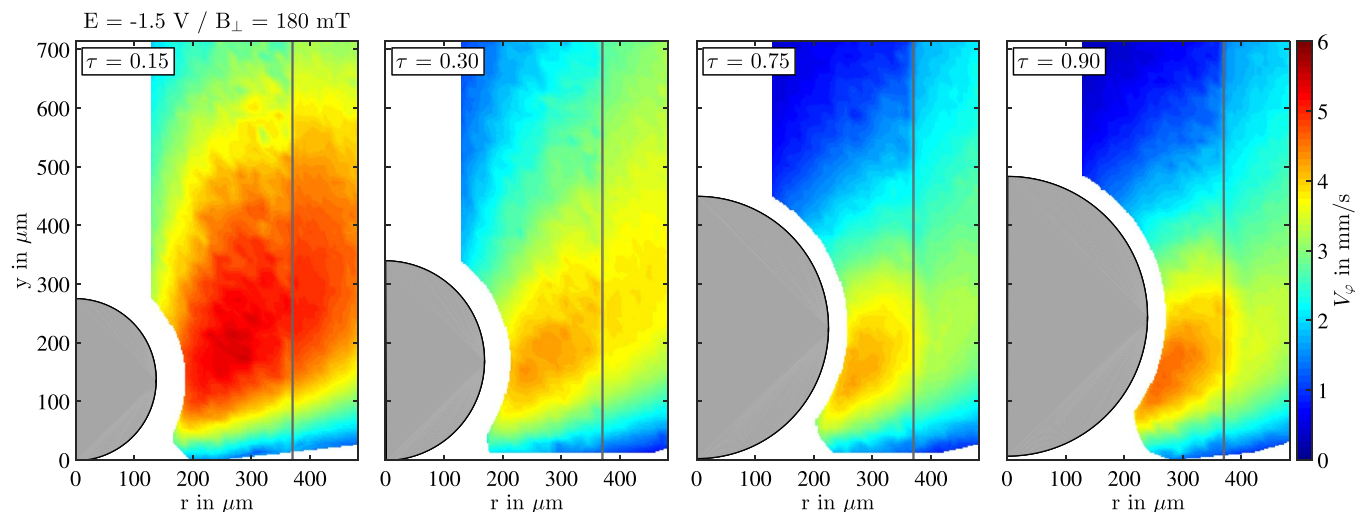
Figure 7. Phase-averaged bubble geometry and velocity fields of the reconstructed azimuthal velocity component V_φ in the presence of a magnetic field for a potential of $E = -1.5$ V and different characteristic phases $\tau = \Delta t/t_{res}$, where Δt denotes the time that passed since the bubble nucleation and $t_{res} \approx 0.3$ s is the residence time of the bubble on the microelectrode, respectively. The size of the phase intervals (bin size) was $\Delta \tau = 0.05$. The data on the left and right side of the vertical line was obtained from the measurements with the measurement plane located 130 μm and 330 μm in front the electrode's center, respectively. The white-marked region around the rim of the bubble and below $r < 130$ μm contains no velocity information as these regions were either hidden by the bubbles' shadow or located outside the measurement plane.

entire field of view and a shift of the high velocity region toward the lower part of the bubble (see Fig. 7). The azimuthal flow on the upper part of the bubble becomes very slow in the last stages of the bubble growth, e.g., for $\tau = 0.75$ and 0.90.

Comparing the steady numerical simulations for the same conditions at $\tau = 0.15$ (see Fig. 9a), the computed azimuthal velocities are generally in good agreement with the experimental data shown in Fig. 7. The upper extension of the high azimuthal velocity region is slightly smaller in the numerical simulation, which can be easily explained by the fact that the steady simulation did not include inertial effects of the flow. In addition, the wake of the preceding bubble is
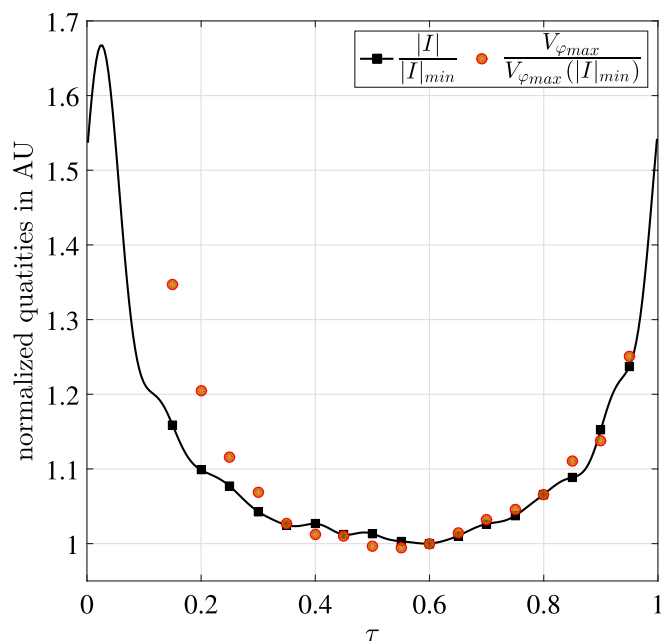
strong during the initial bubble growth phase and might contribute to the resulting azimuthal velocity distribution by transporting fluid of high azimuthal velocity from the lower part of the bubble to the upper part (see also Fig. 10a). However, the influence of the wake was not modeled here as it is only relevant during the very first growth stages[27] and is insignificant for the bubble detachment.

The establishment of a region of high azimuthal velocity in the lower half of the bubble is associated with a pressure decrease in this area. This would lead to a stabilizing effect that retards the bubble detachment rather than accelerating it, which was also suggested by other studies.[29,31] An estimation of this force can be obtained from the numerical data as both the simulation and the experiment provide sufficiently similar distributions of the predominant azimuthal velocity. The hydrodynamic pressure force can be calculated by integrating the relative pressure change along the bubble surface, $F_{\Delta p} = \int_{S_B} (p - p_c) n \, dA$,[24,44] where p, p_c and S_B denote the hydrodynamic pressure in the liquid, the pressure at the contact point of the bubble and the solid surface and the bubble surface exposed to the liquid. As exemplified in Fig. 9, the Lorentz-force-induced pressure difference around the bubble is relatively small (<50 mPa), which yields only a weak stabilizing force of $F_{\Delta p} = 1.56 \times 10^{-9}$ N and 4.3×10^{-9} N for $\tau = 0.15$ and $\tau = 0.9$, respectively. By comparison, the capillary force[24] ($F_C = 2\pi r_c \sigma \sin \theta$)[f], which keeps the bubble attached to the electrode, is several orders of magnitude larger. This can be shown from the experimental data using the corresponding bubble radii with contact angles of $\theta = 9° \pm 3°$ and $\theta = 5° \pm 3°$ for $\tau = 0.15$ and $\tau = 0.9$, which yields $F_{\Delta p}/F_c = 0.05 - 0.2$ % and $0.2 - 3.3$ %, respectively. Consequently, the hydrodynamic pressure force imposed by the Lorentz-force-driven convection is presumably insignificant with respect to a force balance during the entire bubble evolution and thus not able to retard the bubble detachment substantially. Hence, for a comparable range of current densities and magnetic field strengths, the presented experimental and numerical results do not indicate a significant stabilizing effect by the mechanism proposed in the literature. Other mechanisms that may occur in a magnetic field and might affect the bubble growth or current characteristics, such as local phenomena at the contact point at the foot of the bubble or an enhanced mass transfer, should be therefore considered as well.

Figure 8. Evolution of the normalized cathodic current $|I|/|I|_{min}$ and the maximum azimuthal velocity normalized by its value corresponding to the point in time of the minimum cathodic current $V_{\varphi max}/V_{\varphi max}(|I|_{min})$. $\tau = \Delta t/t_{res}$ denotes the phase as described in Fig. 7.

^{f}Surface tension $\sigma = 0.073$ N/m; contact angle θ; contact radius $r_c = \frac{d}{2} \sin \theta$, assuming a circular bubble.

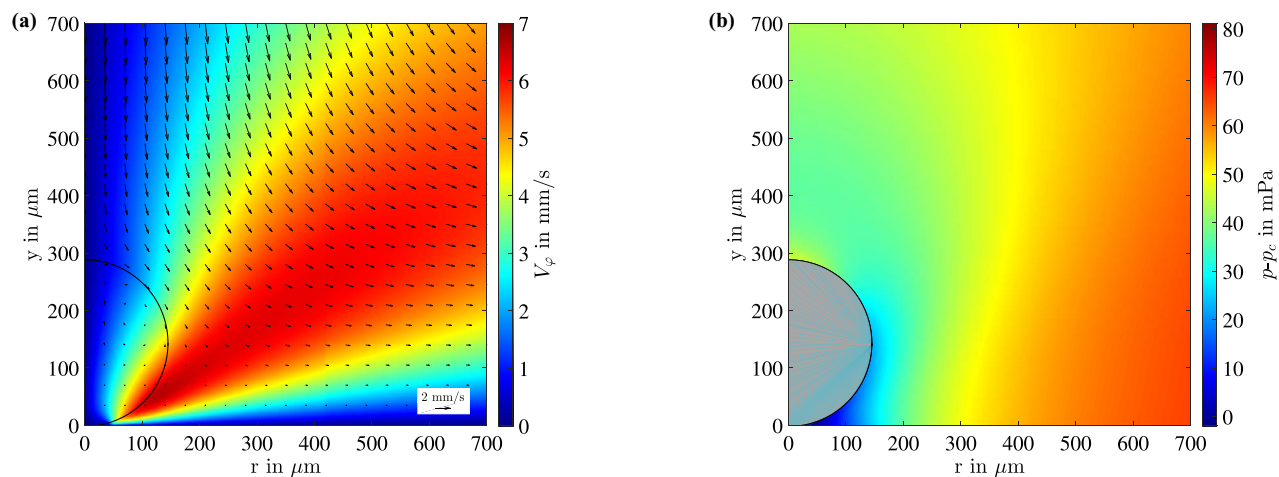**Figure 9.** Zoom into numerical results for E = −1.5 V and $B_\perp \approx 180$ mT at τ = 0.15 (τ denotes the phase as described in Fig. 7): (a) Azimuthal velocity distribution (contour) and velocity vector field in the meridional (r-y) plane; (b) Relative pressure distribution $p - p_c$, where p is the hydrodynamic pressure and p_c denotes the pressure in the liquid at the contact point of the bubble and the solid surface at $y = 0$ mm, respectively. The solid line in (a) and (b) represents the gas-liquid interface.
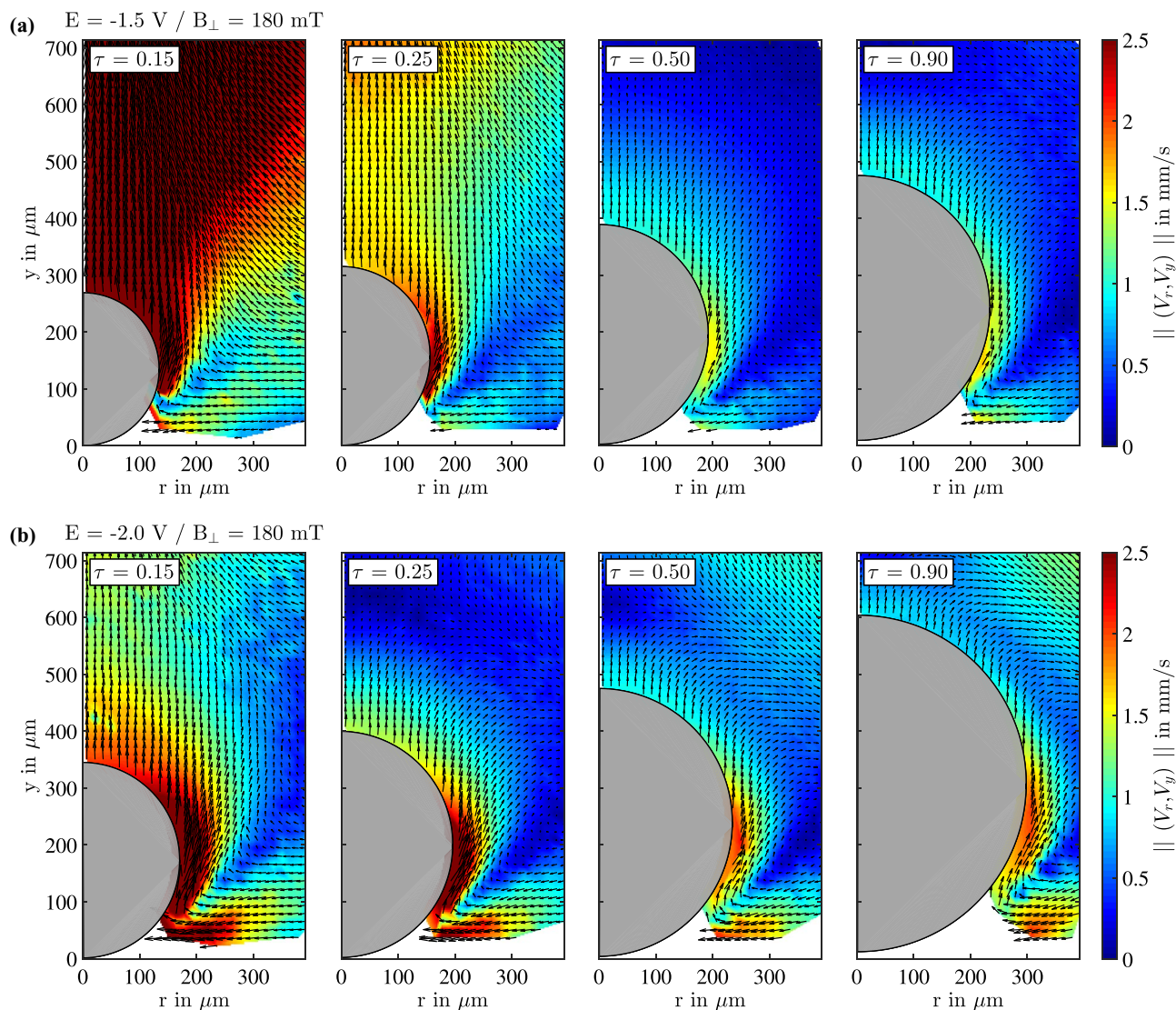

Figure 10. Phase-averaged bubble geometry and velocity fields in the meridional (r-y) plane (V_r, V_y) for different potentials and characteristic phases τ = $\Delta t / t_{res}$ as described in Fig. 7. The residence time of the bubbles on the electrode was about 0.3 s and 0.4 s for E = −1.5 V (a) and −2.0 V (b), respectively. The white-marked region contains no velocity information as no particles could be tracked in these regions.

Fig. 10 depicts the phase-averaged meridional velocity fields obtained from the measurements in the center plane. As was shown by Yang et al.,[27] the electrolyte flow in the absence of a magnetic field is governed by the wake of the previously detached bubble.[27] However, the effect of this wake decays rapidly and has virtually no effect on the bubble growth, except for the very first stages, where the wake-induced convection in the vicinity of the electrode is very strong and enhances the mass transfer toward the electrode. In general, the strong wake can also be observed when a magnetic field is applied (see Fig. 10a) but decays much faster due to the counter-acting effect of the centrifugal acceleration that the fluid experiences during the azimuthal motion. This is particularly evident at a potential of E = −2.0 V, where the effect of the wake vanishes rapidly as the centrifugal forces increase with V_φ^2. Moreover, the secondary flow, i.e. the large vortex that was visible in the bulk (Fig. 6), emerges in the upper right corner of Fig. 10b. In contrast to the observations at E = −1.5 V (see Fig. 10a), such secondary flow can also be seen from the numerical simulations at the same conditions, even in the early phases of the bubble growth (see Fig. 9a). The numerical simulation did not include the influence of the wake, thus the flow is only subjected to the centrifugal acceleration causing the outward directed flow. This demonstrates once again that a significant MHD-induced secondary flow can be only established if the acting Lorentz forces are sufficiently strong to overcome the influence of the wake of the preceding bubble.

Another interesting phenomenon appears on the lower half of the bubble in Figs. 10a and 10b. Here, a significant inward flow toward the foot of the bubble accompanied by an upward flow tangential to the bubble surface can be observed. This effect seems to become stronger with increasing current density/potential and is particularly significant in the early phases of the bubble growth. However, it is unlikely that this is a secondary effect of the imposed azimuthal motion as such comparable flow is not evident from the numerical simulation (see Fig. 9a). It is interesting to note that the tangential flow along the bubble surface shows an increasing magnitude toward the surface. This indicates a flow that is driven by the motion of the bubble's surface, in case of which the inward flow directed toward the foot would simply replace the fluid that was displaced along the bubble surface (conservation of mass). The motion of the interface between different phases might be related to the Marangoni effect, which occurs due to surface tension gradients resulting from concentration or temperature gradients along the interface. However, at this point there is no explanation that would link the occurrence of a Marangoni effect to the magnetic field and the numerical simulations do not include surface driven flows yet. Therefore, the observed flow and its origin has to be further investigated in future experimental and numerical studies.

The velocity measurements clearly demonstrate that the secondary MHD flow can enhance the mass transfer between the electrolyte in the bulk and the near-bubble region (see Fig. 10b and Fig. 6). Such secondary flow and also the local flow phenomena observed close to the foot of the bubble may change the concentration of dissolved hydrogen at the bubble foot and around the bubble surface [14,45] and, consequently, influence the bubble growth.[46,47] This is different to the case without a magnetic field, where the preceding bubble can only induce a convective mass transfer right after its detachment in the initial growth phase of the next bubble.

Summary

The time-dependent three-dimensional flow around a hydrogen bubble evolving at a microelectrode under the influence of an electrode-normal magnetic field was experimentally investigated to gain better insight into the possible effects of the natural and MHD convection on the bubble growth and detachment. Supported by numerical simulations, the following conclusions can be drawn:

• For a magnetic induction of 180 mT, the pressure change around the bubble induced by the MHD flow is very small due to the relatively low azimuthal flow velocities and has therefore only a weak stabilizing effect on the bubble detachment.

• The numerical simulations are in good agreement with the experiment and provide a good framework for future numerical studies. In particular, the observed velocities are several orders of magnitude lower than in a recent numerical study.[31] Furthermore, the measurements indicate a mobile gas-liquid interface and flow inside the bubble which was not considered in previous numerical studies.

• Depending on the magnitude of the Lorentz force, the secondary flow can enhance the mass transfer in the entire cell and toward the growing bubble. Furthermore, a strong meridional convection that was not observed before occurs in the vicinity of the bubble's foot. These flow phenomena might change the local concentration of dissolved hydrogen close to the electrode and around the bubble.

The results improve the current understanding of mass transfer related MHD phenomena and indicate the presence of other interesting interfacial phenomena that should be taken into account in future studies investigating the bubble evolution and detachment characteristics under the influence of a magnetic field.

References

1. D. Pletcher and X. Li, Prospects for alkaline zero gap water electrolysers for hydrogen production, *Int. J. Hydrogen Energy*, **36**, 15089 (2011).
2. H. Vogt, In *Electrodics: Transport*, E. Yeager, J. Bockris, B. Conway, and S. Sarangapani, Eds. Comprehensive Treatise of Electrochemistry, Plenum Press: Ney York and London, Vol. 6, 445–489 (1983).
3. P. J. Sides, In *Modern Aspects of Electrochemistry*, R. White, J. Bockris, and B. Conway, Eds. Plenum Press: New York, Vol. 18, 303–354 (1986).
4. N. Nagai, M. Takeuchi, T. Kimura, and T. Oka, Existence of optimum space between electrodes on hydrogen production by water electrolysis, *Int. J. Hydrogen Energy*, **28**, 35 (2003).
5. H. Vogt and R. Balzer, The bubble coverage of gas-evolving electrodes in stagnant electrolytes, *Electrochim. Acta*, **50**, 2073 (2005).
6. M. Wang, Z. Wang, X. Gong, and Z. Guo, The intensification technologies to water electrolysis for hydrogen production - A review, *Renewable Sustainable Energy Rev.*, **29**, 573 (2014).
7. F. Hine, M. Yasuda, R. Nakamura, and T. Noda, Hydrodynamic Studies of Bubble Effects on the IR-Drops in a Vertical Rectangular Cell, *J. Electrochem. Soc.*, **122**, 1185 (1975).
8. F. Hine and K. Murakami, Bubble Effects on the Solution IR Drop in a Vertical Electrolyzer under Free and Forced Convection, *J. Electrochem. Soc.*, **127**, 292 (1980).
9. C. Sillen, The Effect of Gas Bubble Evolution on the Energy Efficiency in Water Electrolysis. Ph.D. thesis, TU Eindhoven, (1983).
10. B. E. Bongenaar-Schlenter, L. J. J. Janssen, S. J. D. van Stralen, and E. Barendrecht, The effect of the gas void distribution on the ohmic resistance during water electrolytes, *J. Appl. Electrochem.*, **15**, 537 (1985).
11. J. Eigeldinger and H. Vogt, The bubble coverage of gas-evolving electrodes in a flowing electrolyte, *Electrochim. Acta*, **45**, 4449 (2000).
12. B. J. Balzer and H. Vogt, Effect of electrolyte flow on the bubble coverage of vertical gas-evolving electrodes, *J. Electrochem. Soc.*, **150**, E11 (2003).
13. L. M. A. Monzon and J. M. D. Coey, Magnetic fields in electrochemistry: The Lorentz force: A mini-review, *Electrochem. Commun.*, **42**, 38 (2014).
14. T. Iida, H. Matsushima, and Y. Fukunaka, Water electrolysis under a magnetic field, *J. Electrochem. Soc.*, **154**, E112 (2007).
15. Z. Diao, P. A. Dunne, G. Zangari, and J. M. D. Coey, Electrochemical noise analysis of the effects of a magnetic field on cathodic hydrogen evolution, *Electrochem. Commun.*, **11**, 740 (2009).
16. H. Matsushima, T. Iida, and Y. Fukunaka, Observation of bubble layer formed on hydrogen and oxygen gas-evolving electrode in a magnetic field, *J. Solid State Electrochem.*, **16**, 617 (2012).
17. H. Matsushima, T. Iida, and Y. Fukunaka, Gas bubble evolution on transparent electrode during water electrolysis in a magnetic field, *Electrochim. Acta*, **100**, 261 (2013).
18. J. A. Koza, M. Uhlemann, A. Gebert, and L. Schultz, Desorption of hydrogen from the electrode surface under influence of an external magnetic field, *Electrochem. Commun.*, **10**, 1330 (2008).
19. J. A. Koza, S. Mühlenhoff, M. Uhlemann, K. Eckert, A. Gebert, and L. Schultz, Desorption of hydrogen from an electrode surface under influence of an external magnetic field - In-situ microscopic observations, *Electrochem. Commun.*, **11**, 425 (2009).

20. J. A. Koza, S. Mühlenhoff, P. Żabiński, P. Nikrityuk, K. Eckert, M. Uhlemann, A. Gebert, T. Weier, L. Schultz, and S. Odenbach, Hydrogen evolution under the influence of a magnetic field, *Electrochim. Acta*, **56**, 2665 (2011).
21. D. Baczyzmalski, T. Weier, C. J. Kähler, and C. Cierpka, Near-wall measurements of the bubble- and Lorentz-force-driven convection at gas-evolving electrodes, *Exp. Fluids*, **56**, 162 (2015).
22. T. Weier and S. Landgraf, The two-phase flow at gas-evolving electrodes: Bubble-driven and Lorentz-force-driven convection, *Eur. Phys. J.: Spec. Top.*, **220**, 313 (2013).
23. J. Klausner, R. Mei, D. Bernhard, and L. Zeng, Vapor bubble departure in forced convection boiling, *Int. J. Heat Mass Transfer*, **36**, 651 (1993).
24. G. Duhar and C. Colin, Dynamics of bubble growth and detachment in a viscous shear flow, *Phys. Fluids*, **18**, 077101 (2006).
25. T. Weier, S. Landgraf, and C. Cierpka, Über die Lorentzkraft-getriebene dreidimensionale Strömung um eine magnetische Kugel in einem elektrischen Feld. Fachtagung "Lasermethoden in der Strömungsmesstechnik", Dresden, Germany, September 8-10. 2015.
26. L. Luo and H. S. White, Electrogeneration of Single Nanobubbles at Sub-50-nm-Radius Platinum Nanodisk Electrodes, *Langmuir*, **29**, 11169 (2013).
27. X. Yang, F. Karnbach, M. Uhlemann, S. Odenbach, and K. Eckert, Dynamics of Single Hydrogen Bubbles at a Platinum Microelectrode, *Langmuir*, **31**, 8184 (2015).
28. D. Fernández, P. Maurer, M. Martine, J. M. D. Coey, and M. E. Möbius, Bubble formation at a gas-evolving microelectrode, *Langmuir*, **30**, 13065 (2014).
29. D. Fernández, M. Martine, A. Meagher, M. E. Möbius, and J. M. D. Coey, Stabilizing effect of a magnetic field on a gas bubble produced at a microelectrode, *Electrochem. Comm.*, **18**, 28 (2012).
30. H. Liu, L. Pan, and J. Wen, Numerical simulation of hydrogen bubble growth at an electrode surface, *Can. J. Chem. Eng.*, **94**, 192 (2016).
31. H. Liu, L. Pan, H. Huang, Q. Qin, P. Li, and J. Wen, Hydrogen bubble growth at micro-electrode under magnetic field, *J. Electroanal. Chem.*, **754**, 22 (2015).
32. C. Cierpka, R. Segura, R. Hain, and C. J. Kähler, A simple single camera 3C3D velocity measurement technique without errors due to depth of correlation and spatial averaging for microfluidics, *Meas. Sci. Technol.*, **21**, 045401 (2010).
33. N.-T. Nguyen and S. T. Wereley, *Fundamentals and applications of microfluidics*, Artech House, (2002).
34. C. Cierpka, M. Rossi, R. Segura, and C. J. Kähler, On the calibration of astigmatism particle tracking velocimetry for microflows, *Measurement, Science & Technology*, **22**, 015401 (2011).
35. C. Cierpka, B. Lütke, and C. J. Kähler, Higher order multi-frame Particle Tracking Velocimetry, *Experiment in Fluids*, **54**, 1533 (2013).
36. K. Ohmi and H.-Y. Li, Particle-tracking velocimetry with new algorithms, *Meas. Sci. Technol.*, **11**, 603–616 (2000).
37. J. Duncan, D. Dabiri, J. Hove, and M. Gharib, Universal outlier detection for particle image velocimetry (PIV) and particle tracking velocimetry (PTV) data, *Meas. Sci. Technol.*, **21**, 057002 (2010).
38. G. Mutschke, K. Tschulik, M. Uhlemann, and J. Froehlich, Numerical simulation of the mass transfer of magnetic species at electrodes exposed to small-scale gradients of the magnetic field, *Magnetohydrodynamics*, **51**, 369 (2015).
39. COMSOL Physics Reference Manual, Version 4.4, www.comsol.com, Nov. 2013.
40. H. Verhaart, R. De Jonge, and S. Van Stralen, Growth rate of a gas bubble during electrolysis in supersaturated liquid, *Int. J. Heat Mass Transfer*, **23**, 293 (1980).
41. C. Cierpka, T. Weier, G. Gerbeth, M. Uhlemann, and K. Eckert, Copper deposition and dissolution in seemingly parallel electric and magnetic fields: Lorentz force distributions and flow configurations, *J. Solid State Electrochem.*, **11**, 687 (2007).
42. S.-Y. Lin, K. McKeigue, and C. Maldarelli, Diffusion-controlled surfactant adsorption studied by pendant drop digitization, *AIChE J.*, **36**, 1785 (1990).
43. S. Takagi and Y. Matsumoto, Surfactant effects on bubble motion and bubbly flows, *Annu. Rev. Fluid Mech.*, **43**, 615 (2011).
44. G. Thorncroft and J. F. Klausner, Bubble forces and detachment models, *Multiphase Sci. Technol.*, **13**, 35 (2001).
45. H. Matsushima, D. Kiuchi, and Y. Fukunaka, Measurement of dissolved hydrogen supersaturation during water electrolysis in a magnetic field, *Electrochim. Acta*, **54**, 5858 (2009).
46. H. Vogt and K. Stephan, Local microprocesses at gas-evolving electrodes and their influence on mass transfer, *Electrochim. Acta*, **155**, 348 (2015).
47. H. Vogt, On the supersaturation of gas in the concentration boundary layer of gas evolving electrodes, *Electrochim. Acta*, **25**, 527 (1980).